Activation of acceptor levels in Mn implanted Si by pulsed laser annealing

Li, L.; Bürger, D.; Shalimov, A.; Kovacs, G. J.; Schmidt, H.; Zhou, S.;

Originally published:

March 2018

Journal of Physics D: Applied Physics 51(2018), 165304

DOI: https://doi.org/10.1088/1361-6463/aab5a6

Activation of acceptor levels in Mn implanted Si by pulsed laser annealing

Lin Li[1], Danilo Bürger[2], Artem Shalimov[3], Gy. J. Kovacs[3], Heidemarie Schmidt[2,4], Shengqiang Zhou[3]

[1]Department of Physics and Electronics, School of Science, Beijing University of Chemical Technology, Beijing 100029, China

[2]Material Systems for Nanoelectronics, Chemnitz University of Technology, 09126 Chemnitz, Germany

[3]Institut für Ionenstrahlphysik und Materialforschung, Helmholtz-Zentrum Dresden-Rossendorf (HZDR), P. O. Box 510119, 01314 Dresden, Germany

[4]Leibniz Institute for Photonic Technologies (IPHT), 07745 Jena, Germany

In this paper, we report the magnetic and electrical properties of Mn implanted nearly intrinsic Si wafers after subsecond thermal treatment. Activation of acceptors is realized in pulsed laser annealing (PLA) films with a free hole concentration of 6.29×10^{20} cm^{-3} while the sample annealed by rapid thermal annealing (RTA) shows n-type conductivity with a much smaller free electron concentration in the order of 10^{15} cm^{-3}. Ferromagnetism is probed for all films by a SQUID magnetometer at low temperatures. The formation of ferromagnetic $MnSi_{1.7}$ nanoparticles which was proven in RTA films can be excluded in Mn implanted Si annealed by PLA.

1. Introduction

Diluted ferromagnetic semiconductor (DMS) has been a major focus of research recently due to its potential application in spintronics [1]. The magnetic properties of DMS can be controlled by manipulating free carriers via electrical gating, as for controlling the electrical properties in conventional semiconductors [2]. GaMnAs DMS has been a great success due to two facts: (1) the efficient suppression of Mn-rich precipitates [3] and (2) the large hole concentration created by substitutional Mn ions, which reaches 10^{21} cm^{-3} and influences the Curie temperature following the empirical relation $T_C \sim p^{1/3}$ [4]. If GaMnAs can be a guide, these two prerequisites should be considered when fabricating Si-based DMS. In dependence on their lattice site Mn impurities could act as acceptor or donor in Si, which leads to p-type or n-type conducting Si, respectively. Carrier-mediated ferromagnetism with a Curie temperature of ca. 120 K was predicted if p-type conducting Si contained with 5% Mn and a free hole concentration of 3.5×10^{20} cm^{-3} [5]. With particularly low solubility limitation of Mn in silicon under equilibrium conditions, non-equilibrium methods have to be adopted to incorporate sufficient concentration of Mn impurities on substitutional lattice sites in Si [6-9].

As a Si-technology compatible technique, ion implantation is naturally adapted to fabricate Si:Mn magnetic semiconductors. Bolduc *et al.* reported the ferromagnetism in Mn implanted Si by rapid thermal annealing (RTA) [10, 11], but later on the group observed the formation of $MnSi_{1.7}$ silicide nanoparticles in the same samples [12]. Further experimental works unambiguously confirmed the formation of $MnSi_{1.7}$

precipitates and excluded formation of a diluted ferromagnetic semiconductor [13, 14]. Compared with traditional RTA, pulsed laser annealing (PLA) is better qualified to avoid the formation of Mn-rich precipitates [3,15]. Nevertheless, Mn-rich phases have also been observed in Mn implanted Si annealed by PLA [16]. However, the authors did not address the magnetic or electrical properties in their samples [16]. In this paper we present the magnetic and electrical properties of Mn implanted single-crystal Si (001) wafers. Activation of acceptors was realized in the PLA films with a free hole concentration of 6.29×10^{20} cm^{-3} at 100 K while the sample annealed by RTA show n-type conductivity with a much smaller free electron concentration of 2.80×10^{15} cm^{-3} at 300 K.

2. Experiment

Samples used in this study were prepared from nearly intrinsic, Czochralski-grown single-crystal n-type conducting Si (001) wafers with a resistivity of 5.5×10^{3} ohm·cm at room temperature. Two series of samples were prepared: a) Mn^{+} ions were first implanted at an energy of 300 keV with a fluence of $1\times10^{16}cm^{-2}$ at room temperature. Subsequently the second implantation with Mn was performed at 100 keV with a fluence of 4×10^{15} cm^{-2} at room temperature. Such a combination results in a box-like distribution of Mn in Si with the atomic concentration of 1.7% from the surface to a depth of 400 nm. b) Mn^{+} ions were first implanted at an energy of 60 keV with a fluence of $1\times10^{16}cm^{-2}$ in liquid N_2 surroundings. Whereafter, the second implantation with Mn was performed at 20 keV with a fluence of 2.5×10^{15} cm^{-2} in the same

condition, which leads to a uniform distribution of Mn in Si with the atomic concentration of 7.5% from the surface to a depth of 80 nm. These two series of samples will be distinguished as series a and series b hereafter. During both implantation procedures, the angle between the sample surface normal and the incident beam was set to 7° to reduce channeling effects.

After the process of ion implantation, PLA and RTA were performed respectively for 300 ns with an energy density of 5.4 J/cm^2 and for 5 min at a temperature of 800 ℃ in N_2 atmosphere for series a, while in series b, PLA was carried out for 282 ns with an energy density varying from 3.5 J/cm^2 to 2.5 J/cm^2 (shown in Table I). Magnetic properties were analyzed using a superconducting quantum interference device (SQUID) magnetometer (Quantum Design MPMS). Magnetotransport measurements with the field applied perpendicular to the samples were performed in van der Pauw configuration from 5 to 300 K. The depth profile of Mn and the structure were analyzed by Rutherford Backscattering spectrometry/channeling (RBS) and transmission electron microscopy (TEM) techniques before and after annealing. Synchrotron radiation x-ray diffraction (SR-XRD) was performed at Rossendorf beamline (ROBL) at the European Synchrotron Radiation Facility with monochromatic x-rays of 0.1541 nm wavelength.

3. Results and discussion

Figure 1 gives the distribution of Mn determined by RBS measurements for series a. As estimated by SRIM, a_as-implanted sample would present a uniform distribution

of 1.7% Mn in top 400 nm. But a broad distribution with a peak value of around 0.55% Mn is found in the top 1000 nm in a_as-implanted sample from RBS spectrum. However, such divergence can be expected, considering the low solubility and thus the diffusion at room temperature after irradiation [17]. After PLA the Mn distribution has been dramatically changed: an aggregation of Mn appears in the surface region. Previous studies suggest that after the extremely short duration of pulsed laser, the surface of the wafer became liquid and then re-solidified on ms scale [18, 19]. Similar to the calculation in Ref.15, Mn ions first diffuse deeper during the melting procedure; then excess Mn ions are extracted from the solid phase Si into the liquid phase Si during the re-solidification and finally piled up in the near surface region. Meanwhile, due to the high cooling rate, the re-solidification process is far from equilibrium and thus provides the possibility of diluting Mn ions into Si matrix beyond the solubility. As confirmed by RBS results, a relatively uniform distribution of Mn ions under 1% is observed underneath the precipitation at surface. Similar distribution of Mn atoms is also observed for series b after PLA (not shown here).

In order to clarify the structure, we analyzed these films further by TEM. Images of sample b_PLA-3.5 are presented in Figure 2 as an example: the sample contains crystalline segregations near to its surface (Figure 2 (a)), showing that the sample was molten by the laser pulse and resolidified into two recognizable phases. On the one hand, the Si resolidified epitaxially. The laser annealing did not leave any recognizable interface which could mark the boundary between the molten and non-molten volume. On the other hand, the majority of the Mn formed crystalline

precipitations, which can be identified as Mn_5Si_2 by the SAED patterns in Figure 2 (b). The Mn_5Si_2 forms a non-percolative network of randomly oriented grains, which have a strong dark contrast in bright field images in plane view samples (Figure 2 (c)). These Mn_5Si_2 nanocolumns were confirmed to be paramagnetic by previous studies [20]. In contrast, below such precipitation there are no identifiable precipitates.

Figure 3 (a) reveals the magnetization versus field curves (M-H loops) recorded at 5 K. The linear diamagnetic background of Si substrate has been subtracted for all displayed data. The magnetization is normalized by the number of implanted Mn ions. Both as-implanted samples show a minor loop with a relatively low magnetic moment, which is not surprising since most of the implanted Mn ions are located as interstitials. After the application of the laser pulse, the saturation magnetization is significantly enhanced with a more evident hysteretic behavior in both series, which is comparable to the results in hydrogenated amorphous Si films [20]. Although the hysteresis strongly suggests the existence of ferromagnetic moment, the slowly saturated loops indicate paramagnetic component.

Remanence as a function of temperature was measured for series b to further confirm both paramagnetic and ferromagnetic components as shown in Figure 3 (b). B_as-implanted sample reveals almost rarely remanent moment, indicating there is only paramagnetic or superparamagnetic component. But the non-zero remanence after PLA persisting till 350 K strongly suggests ferromagnetism, which can be a result of activation of substitutional Mn atoms. The curves after PLA are perfectly fitted by a combination of Curie-Weiss law and three-dimensional spin-wave:

$M(T)=C/(T-B)+ M_0(1-AT^{3/2})$, where C is Curie constant and M_0 the zero temperature magnetization [21].

Nevertheless, the magnetization in Figure 3 is underestimated since only parts of Mn ions are activated. In Ref. 21, magnetization is precipitously enhanced by the elimination of carrier traps and dangling bonds, indicating the carrier-mediated ferromagnetism. In our case, the small saturation magnetization per Mn ions can also be attributed to the low concentration of activated acceptors. One the other hand, the inhomogeneous Mn distribution also quenches the contribution from most of the Mn ions [22]. I.e., a direct coupling between neighboring Mn ions can result in antiferromagnetism [23].

Magnetotransport measurements were performed in order to obtain the information of carriers in the implanted regions of silicon. As a reference the magnetotransport properties of the undoped nearly intrinsic, Czochralski-grown single-crystal n-type conducting Si (001) wafer (virgin sample) have also been investigated. Figure 4 shows Hall effect measured at different temperatures of all samples. Due to the high resistance at low temperatures, the information of virgin and as-implanted samples are not available, however, Hall measurements of virgin and as-implanted sample at 300 K are given in the inset of Figure 4 for reference: the virgin sample is highly resistive and slightly n-type with an electron concentration of 8×10^{11} cm^{-3}, while the behavior of as-implanted sample at room temperature is dominated by the substrate. It is clear that all PLA samples show p-type conductivity, compared with n-type conductivity after RTA. The free hole concentration increases to 10^{20} cm^{-3} at 100 K in series b,

indicating the activation of the Mn acceptors by PLA. The information of carrier concentration for all samples is listed in Table 1. If we compare our results with the work in Ge:Mn [24], a large hole concentration is necessary for observation of Anomalous Hall effect (AHE) as a sign of a correlation between magnetization and magnetotransport. However, such a correlation does not appear even with a large hole concentration.

Temperature dependent resistance of series a samples can be seen in Figure 5 (a). The a_as-implanted and a_RTA samples reveal insulator behavior although the resistance is already largely decreased after RTA. After PLA the resistance is further significantly reduced. Below 70 K the resistance is slowly increasing with decreasing temperature, revealing a quasi-metallic behavior. Figure 5 (b) shows the plot of lnR vs. 1/T. One can obtain the thermal activation energy of carriers according to the formula $R=R_0\exp(E_a/k_BT)$, where R_0 is a prefactor, E_a the activation energy and k_B the Boltzmann constant. At temperature below 70 K, an extremely small activation energy (far below 1 meV) has been obtained. In the high temperature range, an activation energy of 17 meV is concluded, which agrees with the value reported in Ref. 25. However, the extremely small activation energy in the low temperature range suggests that different mechanisms (such as hopping) may dominate the conduction behavior at low temperature.

SR-XRD was performed to clarify the origin of ferromagnetism in the PLA samples. By both symmetric beam geometry scan (a_PLA sample is shown in Figure 6(a)) and grazing incidence x-ray diffraction (not shown here) we find no detectable crystalline

nanoparticles. $MnSi_{1.7}$ nanoparticles, which were observed using XRD in RTA films and are the origin of ferromagnetism there [13], can be excluded for the PLA samples in both series. The clear Si(004) peak from crystalline Si without any detectable nanoparticles implies the potential to realize Si:Mn DMS using Mn implantation and PLA.

Figure 6 (b) shows the pseudodielectric function spectra $\mathcal{E}(E) = \mathcal{E}_1(E) + i\mathcal{E}_2(E)$ of series a as determined by spectroscopic ellipsometry (SE) measurements. The undoped Si wafer is shown for comparison. Compared with the undoped sample, the imaginary part of the pseudodielectric function at the critical points is a little bit lowered and broadened after implantation. Such behavior is typical for ion-implanted Si wafers due to the damage of crystalline periodicity [26]. After RTA, the damages are mostly removed. As a result the curve reveals nearly the same pattern as the undoped Si wafer. However, the PLA sample presents a quite different behavior compared to other samples. The largely broadened $\mathcal{E}_2(E)$ peak is very similar to that observed in heavily doped Si [27]. We can conclude that such a broad peak would mainly be the increased free-carrier effect after laser annealing.

4. Conclusions

In conclusion, Mn implanted Si wafers were annealed by PLA and RTA. Mn implantation at room temperature and RTA favor formation of Mn clusters. The Mn cluster formation can be avoided by N_2 cooling during Mn implantation and by PLA. The PLA samples in both series present ferromagnetism and electrically activated

acceptors with a relatively high free hole concentration of 6.29×10^{20} cm^{-3} at 100 K in series b. By SR-XRD, no crystalline secondary phase could be detected in the PLA samples within the detection limit. Therefore, one can speculate the ferromagnetism in the PLA samples is hole-mediated.

Acknowledgement

The work is supported by the National Natural Science Foundation of China (Grant No. 11405007). The work at HZDR is financially supported by DFG (ZH 225/6-1).

References

[1] T. Dietl and H. Ohno, Rev. Mod. Phys. **86** 187 (2014).

[2] D. Chiba, M. Sawicki, Y. Nishitani, Y. Nakatani, F. Matsukura and H. Ohno, Nature **455** 515-8 (2008).

[3] M. A. Scarpulla, O. D. Dubon, K. M. Yu, O. Monteiro, M. R. Pillai, M. J. Aziz, and M. C. Ridgway, Appl. Phys. Lett. **82**, 1251 (2003).

[4] K. C. Ku, S. J. Potashnik, R. F. Wang, S. H. Chun, P. Schiffer, N. Samarth, M. J. Seong, A. Mascarenhas, E. Johnston-Halperin, R. C. Myers, A. C. Gossard, and D. D. Awschalom, Appl. Phys. Lett. **82**, 2302 (2003).

[5] T. Dietl, H. Ohno, F. Matsukura, J. Cibert, and D. Ferrand, Science **287**, 1019 (2000).

[6] K. E. Newman, and J. D. Dow, Phys. Rev. B **30**, 1929 (1984).

[7] Z. Werner, C. Pochrybniak, M. Barlak, J. Gosk, J. Szczytko, A. Twardowski, A. Siwek, Vaccum 89, 113 (2013).

[8] T. Li, L. Guo, C. Liu, J. Chen, G. Peng, F. Luo, Z. Jiang, Y. Huang, Mater. Sci. Semicond. Process **21**, 1 (2014).

[9] V.V. Rylkov, A.S. Bugaev, O.A. Novodvorskii, V.V. Tugushev, E.T. Kulatov, A.V. Zenkevich, A.S. Semisalova, S.N. Nikolaev, A.S. Vedeneev, A.V. Shorokhova, D.V. Aver′yanov, K.Yu. Chernoglazov, E.A. Gan′shina, A.B. Granovsky, Y. Wang, V.Ya. Panchenkoe, S. Zhou, J. Magn. Magn. Mater. **383**, 39 (2015).

[10] M. Bolduc, C. Awo-Affouda, A. Stollenwerk, M. B. Huang, F. G. Ramos, G. Agnello, and V. P. LaBella, Phys. Rev. B **71**, 033302 (2005).

[11] M. Bolduc, C. Awo-Affouda, A. Stollenwerk, M.B. Huang, F. Ramos, and V.P. LaBella, Nucl. Instrum. Methods Phys. Res. B 242, 367 (2006).

[12] C. Awo-Affouda, M. Bolduc, M. B. Huang, F. Ramos, K. A. Dunn, B. Thiel, G. Agnello, V. P. LaBella, J. Vac. Sci. Technol. A **24**, 1644 (2006).

[13] S. Zhou, K. Potzger, G. Zhang, A. Mücklich, F. Eichhorn, N. Schell, R. Grötzschel, B. Schmidt, W. Skorupa, M. Helm, and J. Fassbender, Phys. Rev. B **75**, 085203 (2007).

[14] S. Yabuuchi, Y. Ono, M. Nagase, H. Kageshima, A. Fujiwara, E. Ohta, Jpn. J. Appl. Phys. **47**, 4487 (2008).

[15] S. Zhou, J. Phys. D: Appl. Phys. **48** 263001 (2015).

[16] N. Peng, C. Jeynes, M. J. Bailey, D. Adikaari, V. Stolojan, R. P. Webb, Nucl. Instrum. Methods Phys. Res. B **267**, 1623 (2009).

[17] D. Gilles, W. Schröter, W. Bergholz, Phys. Rev. B **41**, 5770 (1990).

[18] M. J. Aziz, Metall. Mat. Trans. A **27**, 671 (1996).

[19] D. Recht, M. J. Smith, S. Charnvanichborikarn, J. T. Sullivan, M. T. Winkler, J. Mathews , J. M. Warrender, T. Buonassisi, J. S. Williams, S. Gradečak, M. J. Aziz, J. Appl. Phys. **114**, 124903 (2013).

[20] D. Kwon, H. K. Kim, J. H. Kim, Y. E. Ihm, D. Kim, H.Kim, J. S. Baek, C. S. Kim and W. K. Choo, J. Magn.Magn. Mater. **282**, 240-243 (2004).

[21] J. H. Yao, S. C. Li, M. D. Lan, and T. S. Chin, Appl. Phys. Lett. **94**,072507 (2009).

[22] Q. Xu, S. Zhou, B. Schmidt, A. Mücklich, and H. Schmidt, Nucl. Instrum.

Methods Phys. Res. B **267**, 3558 (2009).

[23] H. Weng, and J. Dong, Phys. Rev. B **71**, 035201 (2005).

[24] S. Zhou, D. Bürger, A. Mücklich, C. Baumgart, W. Skorupa, C. Timm, P. Oesterlin, M. Helm, and H. Schmidt, Phys. Rev. B **81**, 165204 (2010).

[25] S. Ma, Y. Sun, B. Zhao, P. Tong, X. Zhu, and W. Song, Solid State Commun. **140**, 192 (2006).

[26] K. Tsunoda, S. Adachi, and M. Takahashi, J. Appl. Phys. **91**, 2936 (2002).

[27] G. E. Jellison, Jr., S. P. Withrow, J. W. McCamy, J. D. Budai, D. Lubben, M. J. Godbole, Phys. Rev. B **52**, 14607 (1995).

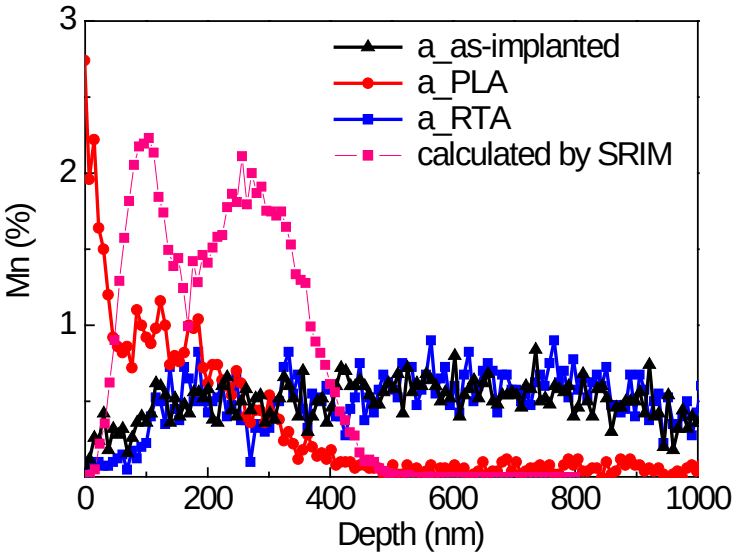

Figure 1 Mn concentration in Si for a_as-implanted, PLA and RTA samples. The Mn distribution calculated by SRIM is also given as a reference.

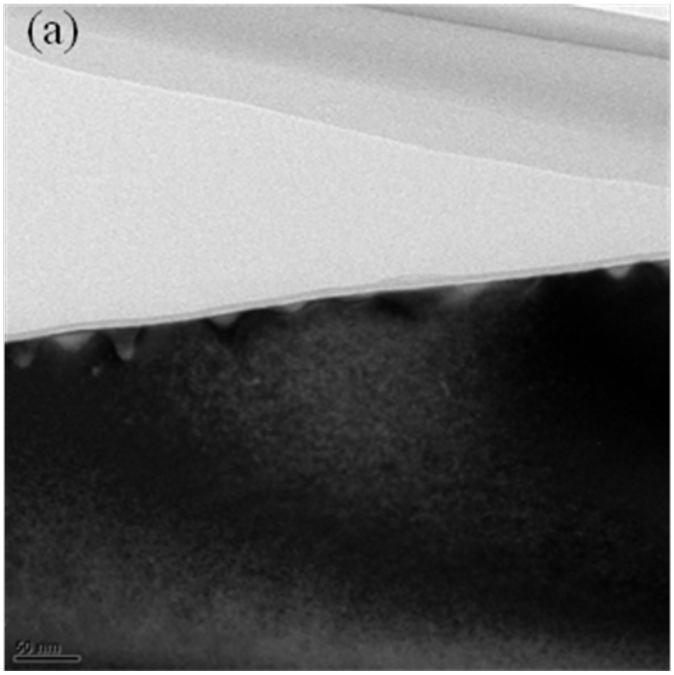

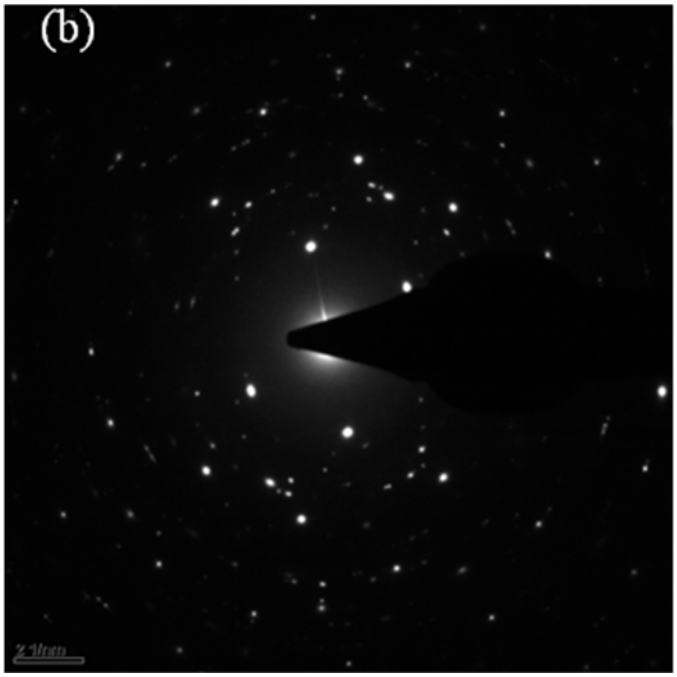

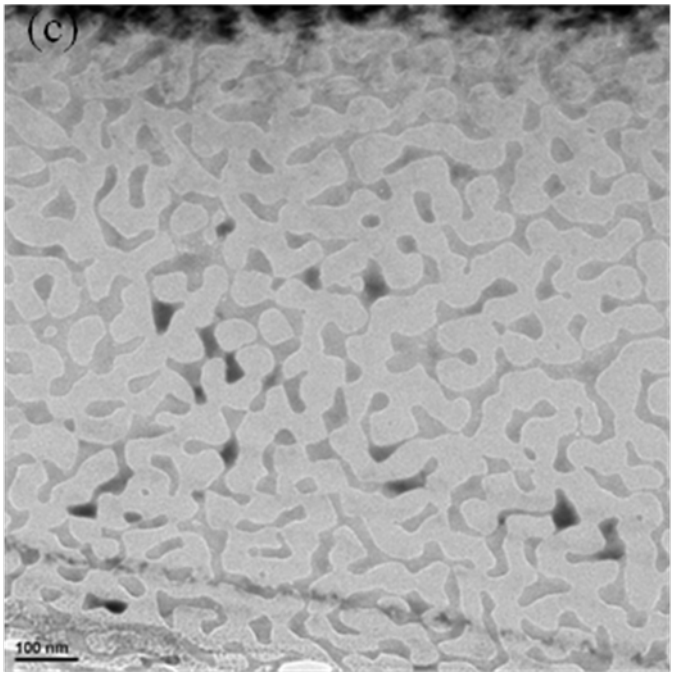

Figure 2 Cross-sectional (a) and plane (c) TEM bright field images, SEAD pattern (b) of sample b_PLA-3.5.

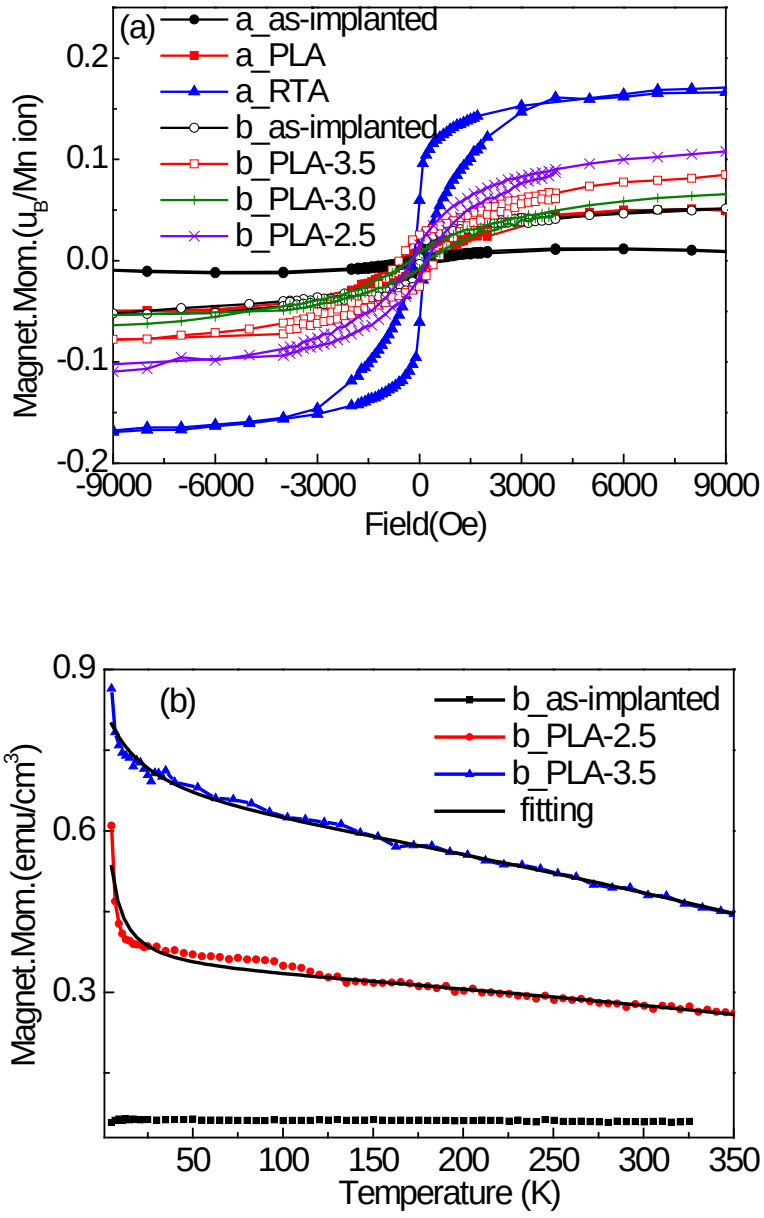

Figure 3 (a) M-H hysteresis loop measured at 5 K of all samples in both series after subtracting the diamagnetic background; (b) Temperature dependent remanent magnetization recorded in a field of 1 mT during warming up the samples.

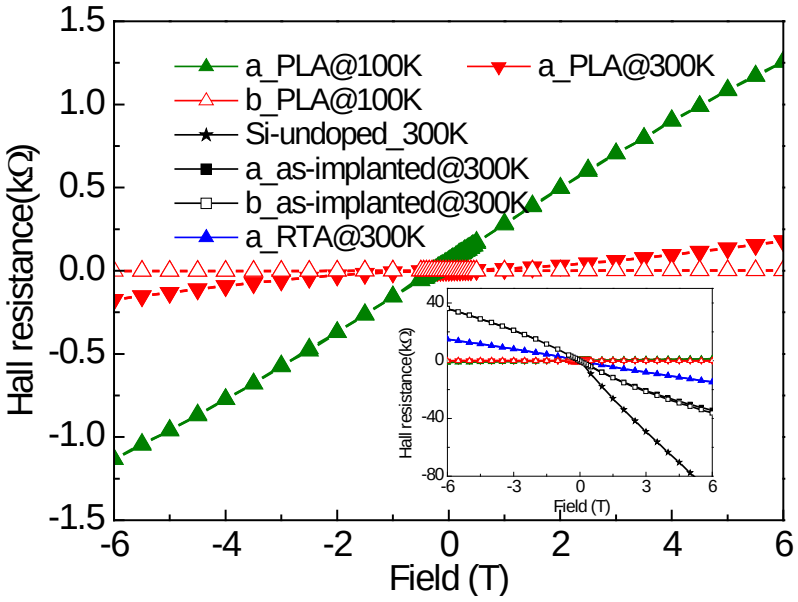

Figure 4 Hall effect measurements of sample a_PLA at 100 K and 300 K, sample b_PLA-3.5 at 100 K. The inset gives results of undoped Si, as-implanted samples of both series and sample a_RTA at 300 K for comparation.

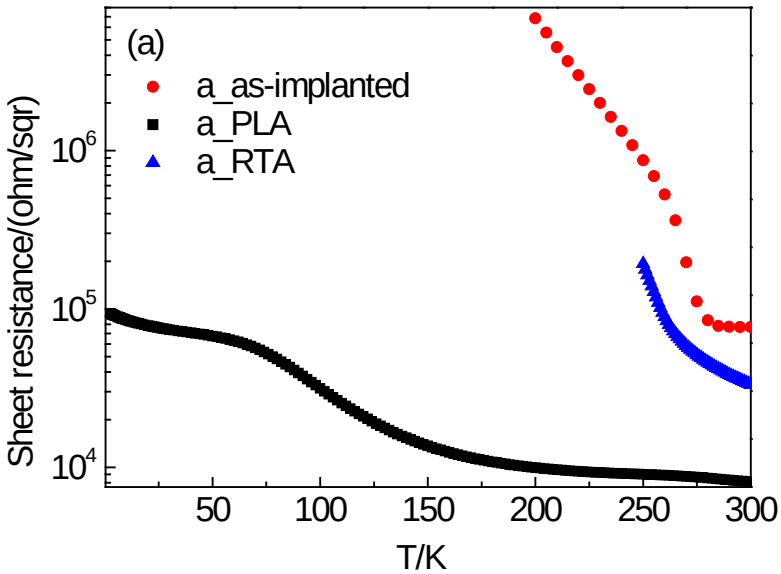

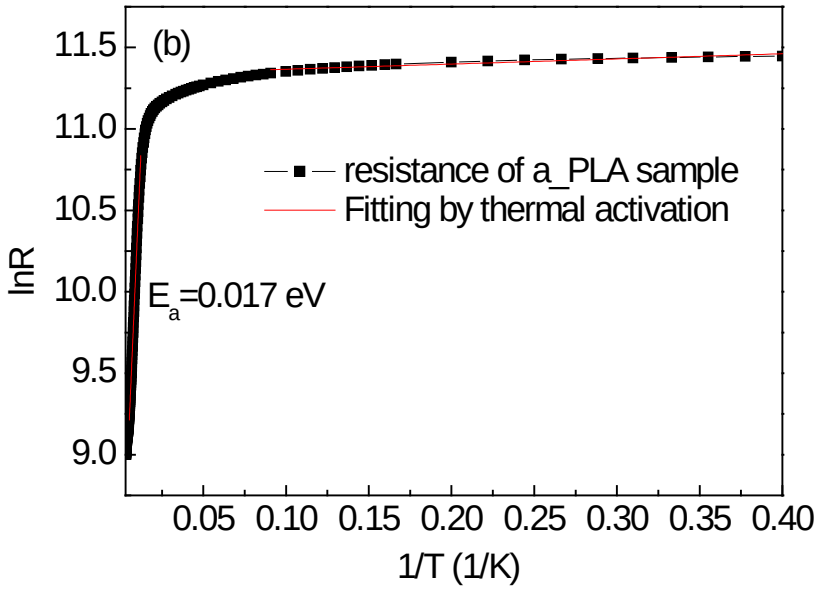

Figure 5 (a) Temperature dependent sheet resistance of the a_as-implanted, PLA and RTA samples; (b) Fitted thermal activation of the a_PLA sample.

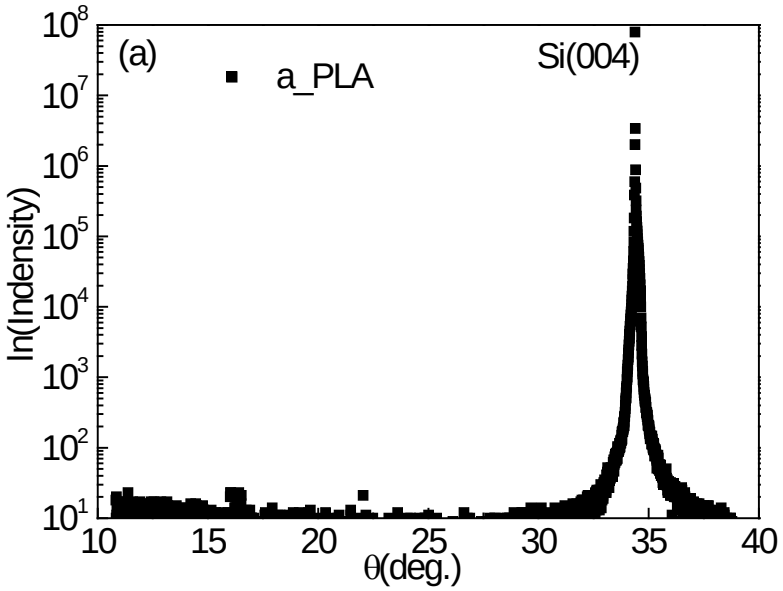

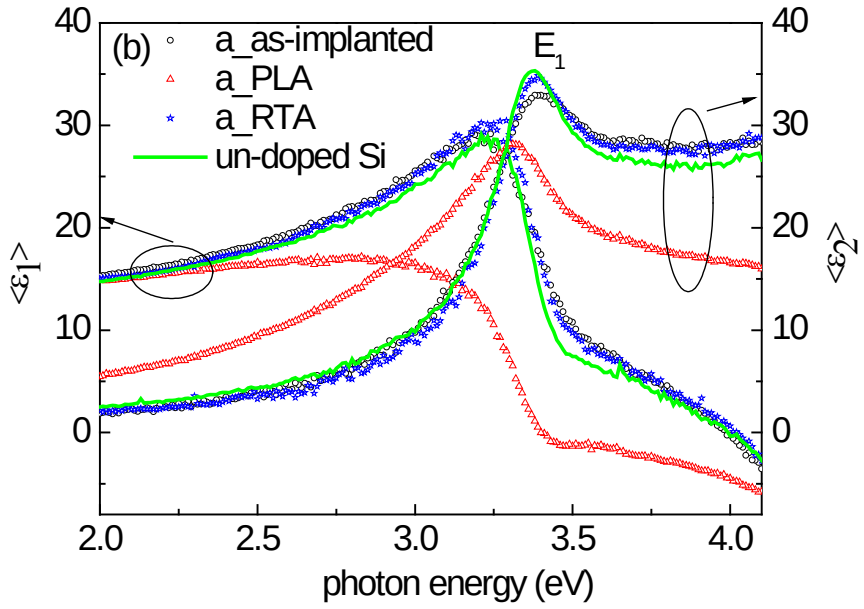

Figure 6 (a) Symmetric beam geometry scan of a_PLA sample by XRD grazing incidence. The peak is from Si (004); (b) Real (ε_1) and imaginary (ε_2) part of the pseudodielectric constant of a_as-implanted, PLA and RTA samples.

Samples	Mn Implantation			Annealing conditions	Carrier concentration ($/cm^3$)
	Energy (keV)	Doses ($/cm^2$)	temperature		
a_as-implanted	300	1.0E16	room	/	-1.41×10^{15} (300 K)
a_RTA	100	4.0E15	temperature	800 ℃, 5 min	-2.80×10^{15} (300 K)
a_PLA				300 ns, 5.4 J/cm^2	$+7.64\times10^{17}$ (300 K)
					$+1.80\times10^{17}$ (100 K)
b_as-implanted	60	1.0E16	liquid N_2	/	-6.46×10^{15} (300 K)
b_PLA-3.5	20	2.5E15	surroundings	282 ns, 3.5 J/cm^2	$+5.72\times10^{20}$ (100 K)
b_PLA-3.0				282 ns, 3.0 J/cm^2	$+6.29\times10^{20}$ (100 K)
b_PLA-2.5				282 ns, 2.5 J/cm^2	$+6.21\times10^{20}$ (100 K)

Table I implantation, annealing conditions and carrier (- electrons, + holes) concentration for PLA samples at 100 K, as-implanted and RTA samples at 300 K.